

On the characterisation of the interfacial toughness in a novel “GaN-on-Diamond” material for high-power RF devices

Dong Liu, Stephen Fabes, Bo-shiuan Li, Daniel Francis, Robert O. Ritchie, and Martin Kuball

ACS Appl. Electron. Mater., **Just Accepted Manuscript** • DOI: 10.1021/acsaelm.8b00091 • Publication Date (Web): 18 Feb 2019

Downloaded from <http://pubs.acs.org> on February 22, 2019

Just Accepted

“Just Accepted” manuscripts have been peer-reviewed and accepted for publication. They are posted online prior to technical editing, formatting for publication and author proofing. The American Chemical Society provides “Just Accepted” as a service to the research community to expedite the dissemination of scientific material as soon as possible after acceptance. “Just Accepted” manuscripts appear in full in PDF format accompanied by an HTML abstract. “Just Accepted” manuscripts have been fully peer reviewed, but should not be considered the official version of record. They are citable by the Digital Object Identifier (DOI®). “Just Accepted” is an optional service offered to authors. Therefore, the “Just Accepted” Web site may not include all articles that will be published in the journal. After a manuscript is technically edited and formatted, it will be removed from the “Just Accepted” Web site and published as an ASAP article. Note that technical editing may introduce minor changes to the manuscript text and/or graphics which could affect content, and all legal disclaimers and ethical guidelines that apply to the journal pertain. ACS cannot be held responsible for errors or consequences arising from the use of information contained in these “Just Accepted” manuscripts.

On the characterisation of the interfacial toughness in a novel “GaN-on-Diamond” material for high-power RF devices

Dong Liu^{*1,2}, Stephen Fabes², Bo-Shiuan Li², Daniel Francis³, Robert O. Ritchie⁴, Martin Kuball¹

¹School of Physics, University of Bristol, Bristol, UK

²Department of Materials, University of Oxford, Oxford, UK

³Akash Systems, San Francisco, USA

⁴Department of Materials Science & Engineering, University of California, Berkeley, and Materials Sciences Division, Lawrence Berkeley National Laboratory, Berkeley, USA

Corresponding author email: dong.liu@bristol.ac.uk

Abstract

GaN thin film integrated to polycrystalline diamond substrates is a novel microwave transistor material with significantly improved heat dissipation capability. Due to the thermal and mechanical properties mismatch between GaN and diamond, a natural concern arises in terms of its interfacial stability as currently there is no established method to evaluate the interfacial toughness in GaN-on-diamond material. Using three generations of “GaN-on-Diamond” materials with varying process parameters, a comprehensive study has been carried out to identify the most appropriate fracture mechanics-based methods for reliable evaluation of the interfacial toughness in this novel material system. Several techniques were assessed and the results are cross-compared; these include an *ex situ* nano-indentation induced buckling method and two-step indentation approach together with several analytical models. Additionally, a micro-cantilever bending method was adopted to measure an upper bound for the interfacial fracture toughness. For the three generation of materials, the interfacial toughness, G_{IC} , was determined to be 0.7, 0.9 and 0.6 J·m⁻², respectively. *Post mortem* analysis of the micro- and nanostructure of fractured interfaces indicated that the systems with better heat spreading capability displayed smoother fracture surfaces, *i.e.*, were more brittle due to the lack of active toughening mechanisms. Potential modifications to the interface for improved mechanical stability has been proposed based on the experimental results.

Keywords: GaN-on-Diamond; Interfacial mechanics; Fracture toughness; Micro-mechanical testing; Nano-indentation; Thin film buckling.

1. Introduction

“GaN-on-Diamond” is a material with great potential for ultra-high power microwave electronics and ultimately for future high-powered monolithic microwave integrated circuits (MMIC), enabling power densities far greater than what is possible with current commercial GaN-on-SiC devices. Applications range from microwave electronics for 5G with several orders of magnitude higher bit rates compared to 4G, satellite-to-earth communication systems to radars where higher power microwave devices will allow significant reduction of blind spots. The underlying reason for the improved performance of GaN-on-Diamond devices is that diamond has a much higher thermal conductivity than SiC, up to 2000 W/mK for diamond vs 450 W/mK for SiC.^{1,2} For example, Pomeroy *et al.*³ reported a 40% decrease in peak channel temperature than in a similar GaN-on-SiC device, comparing the same-to-same device layout. For effective heat-spreading, the diamond is typically less than a micrometre away from the active device area, to maximize heat extraction.

1.1. Manufacture of GaN-on-Diamond and its challenges

There are many ways to produce GaN-on-Diamond materials. The most common method of attaching GaN to diamond was initially performed by Group4Labs^{4,5} (Fig. 1). In this method, the

AlGaIn/GaN active layers are grown on traditional substrates such as Si before attaching the device structure to a carrier wafer (usually Si). A dielectric layer (SiN_x) is then grown onto the GaN, after removal of the original substrate, and used as a seeding bed for the subsequent diamond growth which usually utilizes micro- or nano-size diamond seeds.^{6,7} Wafers can be as large as 4-6 inches.

Alternatively, GaN devices have been directly bonded to diamond⁸ or GaN is grown epitaxially onto single crystal diamond substrates, although the latter approach tends to contain unwanted low-angle grain boundaries and cracks that can compromise device performance. Van Dreumel *et al.*⁹ grew GaN directly onto (100) diamond; Hiramama *et al.*¹⁰ and Alomari *et al.*¹¹ attempted to grow AlGaIn/GaN devices onto (111) diamond, as the 3-fold symmetry of the diamond nearly matches the 6-fold symmetry of (0001) GaN, but this resulted in unsatisfactory thermal properties at the interfacial GaN layer. In all these cases, scaling to the wafer level was challenging.

Accordingly, it has been recognised that the approach of removing the original substrate and growing diamond on GaN is most promising for commercial exploitation. Both hot filament CVD (HF-CVD) diamond as well as microwave plasma assisted CVD (MW-CVD) have been used for GaN-on-Diamond technology though it is easier to achieve a higher thermal conductivity diamond with MW-CVD.^{1,12} As many of the early challenges, involving wafer bow, material quality control and reproducibility, have been effectively solved, the production of GaN-on-Diamond devices is on track to become commercially viable.^{7,13}

Taking full advantage of the diamond thermal properties also requires reducing gate pitch in the devices, which can enable in excess of three times greater power densities and device performance than GaN-on-SiC can provide.^{1,14} Among the many factors that impact the heat sinking capability of GaN-on-Diamond, most pertain to the nature of the interface, in particular the thickness of the diamond nucleation layer SiN_x . For example, as the SiN_x is amorphous it exhibits a low thermal conductivity such that it must be kept as thin as possible¹. This, however, can be technologically challenging, as the SiN_x nucleation layer has to be made much thinner than ~20 nm such that any interfacial flaws will adversely affect its mechanical stability.

Under typical device operation, the temperature at the GaN/Diamond interface ramps between -65°C and 200°C, resulting in interfacial thermal strains due to mismatched thermal coefficients of expansion (GaN $\alpha_a = 5.59 \times 10^{-6} \text{ K}^{-1}$, $\alpha_c = 3.17 \times 10^{-6} \text{ K}^{-1}$; diamond $\alpha = 1.05 \times 10^{-9} \text{ K}^{-1}$). As both materials are stiff (Young's moduli are $E_{\text{dia}} = 1050 \text{ GPa}$ and $E_{\text{GaN}} = 295 \text{ GPa}$), this gives rise to significant local stresses. Therefore, the interface toughness, which characterises its inherent structural integrity to withstand mechanical failure, is critical to the development and reliable operation of this novel material. Despite this, there has been no comprehensive study to date aimed at identifying the most suitable mechanical characterisation methods for this class of GaN-on-Diamond materials. This is the prime rationale for the present study.

1.2 Interfacial mechanics

Many of the methods for the use of interface fracture mechanics for packaging problems were developed in the 1990s.¹⁵ All methods strive to measure a practical adhesion or toughness value rather than the thermodynamic work of adhesion as some plasticity or other energy-dissipating mechanisms always occur. It is considered that such practical toughness values better reflect the "strength" of a dissimilar, or similar material, interface in service.^{15,16} Specifically, the mode I fracture toughness (G_{Ic}) is often quoted as it represents a number that is readily comparable between materials.

Most interfacial mechanics studies have focused on metal-ceramic interfaces, generally for thermal barrier coatings and semiconductor interconnects.¹⁷⁻²² There have been fewer studies

performed on ceramic-ceramic interfaces, or more generally interfaces between two brittle materials, as they are often weak and not engineered to be load-bearing. Modified macroscopic test geometries, such as sandwiched bending tests, first developed by Charalambides *et al.*,^{23,24} and the Brazilian disc with a multilayer at the centre,^{25,26} are popular for the study of interfacial toughness under mode I and mixed-mode conditions, in particular for semiconductor materials.^{19,27} For these types of tests, the sample preparation, either using diffusion or epoxy method to bond the sample to the substrate, has the potential to alter the original material and its fracture behaviour.

Another set of techniques for characterizing the interface toughness have focused on buckling or blistering of thin films; first developed by Dannenberg²⁸, these measure the dimensions of the buckle where G_{Ic} can be obtained.^{16,29} In these cases, indentation methods, either nano- or micro-scale, are employed to cause the buckling. Often the analyses of these experiments require the indent to remain within the film layers,^{30,31} which can limit the achievable plastic driving force for delamination. To resolve this problem, Kriese *et al.*³² used a superlayer which allowed greater indentation depths to be used; the superlayer additionally adds significant compressive stress, making delamination via indentation easier to achieve especially for metallic films on ceramics.^{22,33–36} However, superlayers often can complicate the fracture behaviour; moreover, the harsh deposition conditions may cause unwanted changes to the original interface properties and lead to multiple surface³⁷ and interfacial cracking events that are not necessarily taken into account in the analyses.^{34,38–41}

Several other methods have also been documented, such as scratch tests,³⁵ cross-sectional indentation,^{17,42} micro-wedge indentation^{43,44} and energy-balance techniques techniques,^{45–49} all of which have their own particular advantages and disadvantages for specific applications.

In this work, we utilize an *ex situ* instrumented nano-indentation induced blistering method and employ four analytical models for the interpretation of results, which are evaluated in terms of the input parameters and their limitations for this particular system of a brittle “ceramic-like” film on a stiff substrate. Additionally, a micro-cantilever bending based experimental configuration was developed, based on the He and Hutchinson analysis⁶⁸ of an elastic crack impinging on a dissimilar material interface, in order to provide an evaluation of an upper bound for the interfacial toughness.

2. Experimental Procedures

2.1. Materials

Three generations of GaN-on-Diamond wafers were studied and denoted Gen 1, 2, and 3 according to the iterations of manufacture techniques. Main steps for processing such wafers are shown in **Fig. 1** and general growing conditions can be found in the literature.^{50,51} The thickness of GaN layer varied between 0.7 and 0.9 μm across the wafers with the diamond grown to be $\sim 100\ \mu\text{m}$ thick. The grain size of the diamond was found to be nano-scale near the interface and increases to $\sim 20\ \mu\text{m}$ at the surface of the diamond layer.⁵⁰ The thickness of the SiN_x , the average size of the diamond seeding particles, residual stresses in the GaN film, measured use Raman spectroscopy,⁵² and the thermal boundary resistance (TBR_{eff}) at the interface are shown in Table 1.

In particular, the SiN_x in Gen 2 was abraded with SiC grit paper before seeding whereas in Gen 3 a 5-min ultrasonic bath process was introduced to disperse the particles uniformly. All the samples had an additional protective layer of SiN_x about 10-20 nm on the GaN surface, but it was not considered to affect the indentation process. For the indentation tests, 5 x 5 mm square wafer samples were used. They were cleaned by sonicating in acetone and then ethanol before being mounted onto aluminium JEOL specimen stubs ($E_{\text{Al}} \sim 70\ \text{GPa}$) using a very thin layer of silver ElectroDag (Agar Scientific). The

results were compared to samples mounted by a thin layer of crystalbond glue, and found to be completely consistent which indicated high confidence in the experimental measurements. To limit damage, a holder for these stubs, compatible with the nanoindenter, was designed to allow the samples to be transferred between instruments without demounting the samples.

2.2. Experimental methods

Experiments involved the use of a nanoindenter to cause delamination at the GaN/Diamond interface for the quantification of the interfacial toughness. Specifically, a NanoindenterXP (Agilent technologies) was employed, with a diamond Berkovich tip (Synton-MDP), which has a three-pointed pyramid tip with a half angle of 62.57° . The tip was calibrated at the beginning of the project by making an array of nine indents to a depth of $2\text{ }\mu\text{m}$ in a block of fused silica.

During the indentation, the indenter load was altered by setting a fixed displacement, of 600 to 900 nm, with each displacement repeated 3 to 15 times; a constant strain rate of 0.5 s^{-1} was used throughout. There were two hold periods (Fig. 2a): one at the maximum load to allow the system to settle, the other to measure the thermal drift, which was kept below 0.1 nm s^{-1} . The indents were formed in arrays spaced 50 to $60\text{ }\mu\text{m}$ apart to avoid elastic/plastic interactions between the blisters (Fig. 2b). The maximum load and displacement were taken from the load-displacement curves and the modulus, hardness, and plastic indent depth were extracted using the Oliver and Pharr⁵³ method.

In addition to the monotonic indentation approach described above, a two-step method was also used as described by Lu *et al.*⁴⁸ This involved two loading cycles with a small holding load (5% peak load for 5 s) in between (Fig. 2c). The same tip, as employed for the monotonic loading, was used and the loading and unloading rate was $2000\text{ }\mu\text{N s}^{-1}$ to give a similar strain rate. In the second unloading curve, an 'elbow point' appeared which indicated that the interfacial flaw was being closed. Integrating both curves up to the elbow point and the value on the unloading curve (W_1) for the first indent was subtracted from that of the second indent (W_2) to give the work of delamination (Fig. 2d).

After indentation, atomic force microscopy (AFM) was used to measure the dimension of the blisters. An AFM 5400 (Agilent Technologies, Oxford Materials Characterisation Service) was used with aluminium-coated silicon tips (Mikromasch). The tips were 12-18 μm in height with a conical half-angle of 8° (uncoated). Scanned areas were typically $\sim 30 \times 30\text{ }\mu\text{m}$; 512 points per line at 0.5 lines per second was used across all indents to maximise accuracy. Some of the indents were also measured using an Olympus BX60M optical microscope, with no polarisation and a 100x lens, to compare with the AFM. Finally, a Zeiss Auriga Focused Ion Beam (FIB) instrument was used to section and examine the Gen 1 material blisters that had been measured with the optical and AFM. 30 kV and a FIB current of 1 nA were used.

For the micro-cantilever bending, specimens were made using a FEI FIB200 and Zeiss Auriga (David Cockayne Centre for Electron Microscopy, Oxford University), on a Gen 1 wafer. The steps for the two methods (M1 and M2) for cutting the cantilevers are shown in Fig. 3. For the larger cuts, a FIB current of 4 or 5 nA was used, with 1 nA for cleaning. To form the notches, 10 pA FIB current was used for 6 seconds to ensure that as sharp a notch as possible was created.

Lastly, transmission electron microscopy (TEM) images were undertaken on Dualbeam Helios FIB milled samples using a FEI Tecnai OSIRIS STEM (150 kV) in each material and the interfacial attachment between GaN, SiN_x and diamond were examined to assist the understanding of the fracture mode at the interface.

The cantilevers were tested using a Nanoindenter-G200 (Agilent Technologies). A Berkovich tip was used to first scan the cantilever, in AFM mode, with 24 x-points and 250 y-points to precisely locate the loading point. A scanning load of 2 μN was used to avoid damaging the cantilevers. During testing the flat edge of the tip was aligned toward the cantilever to ensure bending occurred rather than indentation (Fig. 3b). Cantilevers were loaded slowly during the test, at 4 $\mu\text{N s}^{-1}$, to encourage interfacial failure. After testing the cantilever fracture surfaces were observed in a Zeiss Auriga microscope.

3. Results

3.1. Characterisation of the buckling geometry

First of all, the Young's modulus E and hardness H of the GaN film in all three generations of the GaN-on-Diamond materials were measured; values of $E_{\text{GaN}} = 295 \pm 10$ GPa and $H_{\text{GaN}} = 19.1 \pm 1$ GPa were obtained, similar to those in the literature ($E_{\text{GaN}} = 287\text{--}320$ GPa, $H_{\text{GaN}} = 12\text{--}22$ GPa).^{54,55} As the subsequent analysis is based primarily on the delamination size and the buckle geometry, a reliable method to characterise these parameters had to be established. As the buckling heights for GaN-on-Diamond are much lower than other materials systems such as metal on stiff substrate, it is not possible to directly translate experience from the latter material systems.

As such, three approaches, AFM, optical imaging and FIB cross-sectioning, were used with the results compared. Specifically, for AFM and optical methods, three-line profiles were taken across the indent with a fourth taken away from the indent to calculate the average height of the sample in the AFM data, or average grey level in the optical measurements (Fig. 4a). The standard deviation in this average was derived, and a threshold was set at the average and four (AFM) or six (optical) times the standard deviation. The maximum height of the buckle was then subtracted from the threshold to derive the actual buckle height. The threshold widths were defined where the profile became flat and corrected by adding a slight random error. Other methods, such as using gradient and edge detection were tried; however, the edges of the buckle were not sharp such that these methods did not give reliable results. The AFM data were first planarized, with rows aligned with a median of differences technique, to remove artefacts using Gwyddion software.⁵⁶ It worth noting that the top thin protective layer tended to chip (Fig. 4b); however, when large-scale cracking occurs, the blister/buckle was considered to be "invalid" (Fig. 4c) and no further measurements were taken.

To directly compare the results of AFM and optical measurements, 95 indents were examined; the results from one of samples is presented in Fig. 5a. It was found that the two methods showed good agreement in both the average and uncertainties. However, the FIB results showed a random disagreement with AFM and optical measurements. It was considered that FIB cross-sectioning tends to relax the residual stresses in the buckled layer which leads to closure of the cracks. Considering that optical method could not measure the height of the blisters, we concluded that AFM was the best method for a reliable characterisation of the blister geometry. The size of all valid blisters measured in this work from all three generation of materials are presented in Figs. 5c and 5d where, in addition to a linear relation existing between their height and width, both dimensions displayed a nearly linear relationship with applied load, which is typical for indentation-induced interfacial cracking.^{57–59}

3.2. Interfacial fracture toughness (monotonic loading)

There are three main analytical models in the literature for analysing such buckled blisters, namely the Evans and Hutchinson⁶⁰ (EH) analysis, Marshall and Evans³¹ (ME) analysis and Hutchinson and Suo⁶¹ (HS) analysis. All the models consider the blister as a clamped plate undergoing Eulerian buckling. The critical, biaxial, buckling stress, σ_B is given by:⁶¹

$$\sigma_B = \frac{\mu^2 h^2 E}{12 a^2 (1 - \nu^2)} \quad (1)$$

where h is film height, a is blister radius, E and ν are, respectively, the Young's modulus and Poisson's ratio of the film. The constant μ^2 refers to the buckling format. For a single buckle, $\mu^2 = 14.68$; for a double or annular buckle, $\mu^2 = 42.67$. The implications of this are discussed below in the Discussion section.

The EH and ME analysis focus on the indentation-induced compression (Fig. 6a). The plastic indent volume, V_p , is used to calculate an expansion of the plate, assuming the thickness of the plate is retained and that the indent volume all becomes a radial expansion.^{31,60} This expansion, Δ_o , is given by:^{31,60}

$$\Delta_o = \frac{V_p}{2\pi a h} \quad (2)$$

V_p is calculated using the residual plastic indent depth, d_p .¹⁶ If the indenter tip is assumed to be a perfect triangular pyramid with a Berkovich area function of $24.5d^2$, then:

$$V_p = \frac{24.5}{3} \times d_p^3 \quad (3)$$

The indentation-induced, biaxial, compressive, edge stress is then calculated as:^{31,60}

$$\sigma_o = \frac{E V_p}{[2\pi(1 - \nu) h a^2]} \quad (4)$$

Unlike the EH analysis, the ME analysis includes a consideration of residual stresses.³¹ In both methods, $\sigma_o > \sigma_B$ must be satisfied for buckling to occur. However, this is never achieved in any of the generations of GaN-on-Diamond samples (Fig. 6b), although it is clear that buckling occurred. Therefore, the ME method is clearly not ideal for our bi-material system, possibly because (i) GaN is a brittle anisotropic intermetallic with a Wurtzite crystal structure which could lead to errors in calculating its expansion;⁶² (ii) the ME analysis requires a stiff substrate that can fail due to plastically deforming interlayers;¹⁵ however, the SiN_x layer is thin and unlikely to have failed in this manner; (iii) the analyses are derived for thick metallic films and only consider plasticity-induced edge stresses^{31,60}. With a thin film of a brittle material, the deformation is largely elastic. Waters and Volinsky³⁶ reported ME and HS analyses were ideal for a metal films, suggesting that due to the highly brittle nature of the GaN, the ME and HE analyses are not ideal.

Hutchinson and Suo (HS)⁶¹ tackled the problem in reverse. In their analysis, the final buckle is considered and the driving stress, σ_D , to form such a buckle is then back-calculated. This avoids the assumptions concerning σ_o and means that a residual stress in the film is not required. σ_D is calculated by rearranging the Euler buckling amplitude, B , using the measured buckle height, δ ⁶¹, viz:

$$B = \frac{\delta}{h} = \left[\frac{1}{C_1} \left(\frac{\sigma_D}{\sigma_B} - 1 \right) \right]^{0.5} \quad (5)$$

where, $C_1 = 0.2478(1 + \nu) + 0.2231(1 - \nu^2)$. Rearranging gives:

$$\sigma_D = \sigma_B \left(1 + C_1 \left(\frac{\delta}{h} \right)^2 \right) \quad (6)$$

The mixed-mode interfacial fracture toughness is then calculated using:⁶¹

$$G_{ic}(\psi) = C_2 \left[1 - \left(\frac{\sigma_B}{\sigma_D} \right)^2 \right] \frac{(1-\nu)h\sigma_D^2}{E} \quad , \quad (7)$$

where, $C_2 = [1+0.9021(1-\nu)]^{-1}$.

HS then used an asymptotic solution for the phase angle (an evaluation of the mode mixity at the interface between mode I and mode II in this case), ψ , of a circular blister (the detailed description of phase angle is included in Appendix I):⁶¹

$$\psi = \tan^{-1} \left[\frac{\cos \omega + 0.2486(1+\nu) \frac{\delta}{h} \sin \omega}{-\sin \omega + 0.2486(1+\nu) \frac{\delta}{h} \cos \omega} \right] \quad , \quad (8)$$

where $\omega = 52.1^\circ$.⁶¹ The mode I fracture toughness, G_{Ic} , can then be determined to be:⁶¹

$$G_{Ic} = \frac{G_{ic}(\psi)}{[1 + \tan^2((1-\lambda)\psi)]} \quad , \quad (9)$$

where, $\lambda = 0.3$ describes the shear contribution to the fracture toughness, assuming a brittle interface.⁶¹ This assumption is justifiable as all the spallation surfaces in the present GaN-on-Diamond samples that show brittle interfacial fracture.

It is emphasized that although mixed-mode toughness is most relevant to bi-material interfaces as even if one loads the interface in mode I, the modulus mismatch across the interface will still induce a mode II component, the current work extracted mode I fracture toughness (excluding the shear component at the interface) from the mixed-mode toughness based on the phase angle and compared across materials in this work. However, we accept that the mixed-mode G_{Ic} is likely a 'truer' reflection of the interfacial toughness.

Recall that in Figs. 5c and 5d, the blister radius (a) and height (δ) were shown to have a near linear relationship. Expanding the HS analysis yields $\delta \propto a^{4/3}$, and the index value of 1.28, 1.57 and 1.32, respectively, were obtained from the experimental results for the Gen 1, 2, and 3 GaN-on-Diamond materials. As these index numbers are near 4/3, it suggests the HS prediction aligns better with the experimental results. The calculated interfacial fracture energy is plotted in Fig. 7a. There is a clear trend towards higher G_{Ic} values for smaller blisters, due to the overlapping of the plastic zones around the indent and emanating cracks, which causes inflated G_{Ic} values as the elastic assumptions in the model are no longer met.^{32,63} Accordingly, only long crack (in this case, blister radius is about 10 times of the GaN film thickness) plateau regions were considered to reflect the fracture toughness of the interface. As the average values appear close to one another, an ANOVA statistical analysis was performed (Table 2). The two ANOVA test statistics are F and the P value; as F is much larger than F_{crit} and P is much smaller than the hypothesis value (α) of 0.05, the analysis shows that the three populations and their averages are different. The averaged fracture toughness values for the three materials are listed in Table 3. Note that the 'unpinned' data used $\mu^2 = 14.68$ for single buckle in Eq. (1) while $\mu^2 = 42.67$ for 'pinned' double buckle results. In the GaN-on-Diamond system it is considered the buckles are unpinned, *i.e.*, a single buckle, and this is validated by the two-step method and the micro-cantilever testing. This is discussed further in the Discussion section.

3.3. Interfacial fracture toughness (two-step method)

Two-step method for the measurement of interfacial toughness was first proposed by Xie *et al.*⁴⁶ and builds on the analysis of Hainsworth *et al.*⁴⁵ by conducting two consecutive indentation loading cycles on one site. However, as some clarity on the method was lacking in published literature, the

present work sought to clarify the model's theoretical basis for the use on the GaN-on-Diamond materials, specifically by comparing the results with those derived from the monotonic methods.

In this thermodynamic model, there are three main energies of interest: W is the external work done by the indenter, U_c is the energy related to the crack, and U_E is the elastic strain energy stored in the film.⁴⁵ The external work done by the indenter is given by the area under the load-displacement curve.⁴⁵ Considering the two areas (1 and 2) in Fig. 2d, during the unloading of the first indent, the indenter work is balanced by the elastic strain energy stored in the film and the energy release of the crack. U_c is negative as energy is being released as the crack grows, such that:

$$W_1 = U_{E1} - U_c \quad (10)$$

On reloading, the indenter flexes the film and the indenter work is matched by the elastic strain energy in the deflected film:

$$W_2 = U_{E2} \quad (11)$$

The elastic strain energy in the fully flexed film is then assumed to be equal to the elastic strain energy in the film during the first unloading. This is reasonable as the dimensions of the delaminated film section can be assumed to be equal. To identify the point where the film is fully flexed, the elbow point is found (Fig. 2d),^{46,48} which represents the point where the indenter has closed the interfacial flaw and is pushing on both the film and substrate, rather than the suspended film.⁴⁸

Taking $W_2 - W_1$ and using $U_{E1} \approx U_{E2}$:

$$W_2 - W_1 = U_{E2} - U_{E1} + U_c \approx U_c \quad (12)$$

where U_c is given by:

$$U_c = G_{ic}(\psi)\pi r^2 \quad (13)$$

where $G_{ic}(\psi)$ is the mixed-mode fracture toughness of the interface, and r is the delamination radius. Inserting this into $W_2 - W_1$ and rearranging gives:

$$G_{ic}(\psi) = \frac{W_2 - W_1}{\pi r^2} \quad (14)$$

The model implicitly assumes the majority of crack growth occurs at the end of unloading, due to tensile stresses at the interface. The original authors^{46,48} claimed that these were plasticity-derived, but for GaN-on-Diamond they are likely to be predominantly elastic. In this study, final delamination radii were used for r and no crack growth was assumed to occur during the second loading cycle.

Based on the above understanding, example load-displacement graphs for 75 mN indents are shown in Fig. 8. For the Gen 2 material, the deformation associated with the second indent was essentially elastic (Fig. 8a) while for the Gen 1 and Gen 3 materials, the second loading curve showed some extension and bowing (Fig. 8b) suggestive of further plasticity or crack extension. In general, the Gen 3 indents were deeper due to their thicker GaN layers. The delamination radii from these tests are plotted as a function of the maximum load in Fig. 8c; note that smaller indents were used in two-step method to avoid buckling. There is a plateau at the smallest crack lengths ($< 2 \mu\text{m}$), which could be an indication of a threshold crack length related to the indenter geometry. The work of delamination across the three generations of GaN-on-Diamond material were calculated and plotted as a function of the maximum applied load in Fig. 8d. There is a noticeable dip at 140 mN, which we believe occurs at the onset of buckling or cracking of the protective film.

To derive a mode I toughness ($\psi = 0$) that is comparable with other methods from the mixed-mode fracture toughness G_{Ic} (Eq. 13), a phase angle of the mixed mode is needed; but this was not discussed by the original authors of the two-step method.^{46,48} However, as the system is very similar to lateral cracking in ceramics,^{58,59} a method proposed by Chen *et al.*⁵⁹ was used here to estimate the phase angle based on the lateral crack vs. the plastic-zone radius (R_p).

As such, R_p was derived based on its relationship with the maximum indentation depth, d_m , in the first loading cycle by the following relationship:

$$\frac{R_p}{d_m} = -12.907 \frac{H}{E} + 4.5451 \quad (15)$$

The Mode I fracture toughness, G_{Ic} , is plotted in Fig. 9a with the average data shown in Table 4. ANOVA analysis was performed which suggested that the average values of the three generations of material were different, as deduced in the monotonic method (Table 5). One uncertainty in the analysis of the two-step method came from the circular assumption of the delamination, especially for smaller ones, where the shape of the delaminated area is more asymmetric. This error was assumed to be encompassed in the measurement error of the delamination radii. There was a random error in identifying where the flaw is fully closed, as it is probably past the observed elbow point. Sensitivity analyses showed moving the elbow point within reasonable bounds gave ~10% error in $G_{Ic}(\psi)$. Average values of c/R_p and h/R_p were used to encompass the error in the approximate calculation of the phase angle and plastic zone radius (Table 4). Based on these analysis, the results from the two-step method were found to be consistent with the HS model using an 'unpinned' single buckle assumption.

The final crack population radii obtained from the two-step model were compared with that measured from the monotonic test (Fig. 9b-d). Data points for all the three generations of material lie on the same linear trend, except for the Gen 2 and Gen 3 materials that had a small increase in the crack radius as the two group of data joins. This suggests that only minimal crack growth had occurred in the second loading cycle for the Gen 1 material with potentially only a small increase in crack length in the Gen 2 and 3 samples. None of this, however, had much effect on the calculated fracture toughness results (compare Table 3 and Table 4).

3.4. Interfacial failure mode

It is common practice to section blisters to observe their failure behaviour.^{35,63} However, FIB slices alone were hard to interpret due to the limited field of view. In this work, spalled indents were used to give complimentary information and compare the fracture behaviour between the three generations of GaN-on-Diamond material. As spallation tended to occur after blistering/buckling, it was assumed that the spalled fracture surfaces were representative of the blister fracture at the interface. The three generations of materials showed different fracture behaviours. These were analysed qualitatively to ascertain which fracture and consequent toughening mechanisms were active.

Firstly, both Gen 1 and 3 materials have similar toughness (Table 3 and 4) and fracture modes (Figs. 10a, c) where the crack propagated along both the GaN/SiN_x and SiN_x/Diamond interface by hopping between them. Gen 1 materials presented a roughly similar fraction of failure along both interfaces (Fig. 10a), whereas in the Gen 3 material, failure was more dominated by fracture on one interface (Fig. 10a, 10c). To form these fracture surfaces, the interfacial crack must deflect through the SiN_x layer; indeed, it is evident in Fig. 11b.1 that there were interfacial micro-flaws in Gen 1 wafers to facilitate such deflection. The TEM images of the Gen 1 material (Figs. 11b.2) show clearly the

mechanism behind this fracture mode; specifically, the diamond seeding-particles are less densely packed, which allows the diamond growth environment to etch away the SiN_x leading to the formation of micro-flaws. The uniformly dispersed, smaller seeding-particles of the Gen 3 material (Fig. 11c, c.1) mitigate such flaws from occurring as much less dense distributed flaws were seen. This resulted in a smoother crack path (Fig. 10c) than Gen 1 although small amount of zigzag cracks were present (Fig. 10a). For Gen 1, the presence of interfacial flaws (Fig. 10a.1) facilitate the crack deflection and explained the evenly mixed fracture pattern in the Gen 1 material (Fig. 10a). On the other hand, as the cracks are deflected at the interface, this extrinsic mechanism leads to a slightly higher toughness in the Gen 1 compared to the Gen 3 material. The precise mechanisms here are by the flaws locally blunting their crack tips and/or from the crack deflection leading to crack bridging. Indeed, near the indents (Fig. 10a), the crack deflections look similar to the crack bridges shown by Swanson *et al.*⁶⁴ As the bridges are small and widely spaced, the effect is not large.

The Gen 2 material is the toughest of the three materials; it displays a different fracture pattern in that there is a complex crack path undulating between GaN/ SiN_x and SiN_x /diamond seeding layer (Figs. 10b, 11b, 11b.1, 11b.2). The diamond seeding surface displays a chaotic structure with considerable roughness that would require a higher energy to propagate a crack through the seeding clusters (Fig. 11b.1). Indeed, Miyazato *et al.*⁶⁵ provided evidence where a complex crack path could significantly raise the fracture toughness at an YBCO/Ag interface ($G_{lc} = 80\text{--}120 \text{ J}\cdot\text{m}^{-2}$). In addition, as the cracks must deflect around the clusters of diamond particles, this could lead to crack bridging which could account for the increased toughness of the Gen 2 materials. No secondary fracture around the bridges is seen, as in large-grained ceramics, which limits the effectiveness of the bridging. The origin of the clusters in Gen 2 could be attributed to the scratching of the SiN_x before seeding, which causes the diamond particles to align with the direction of the scratches.

3.5. *In situ* micro-cantilever bending

Micro-cantilevers with the GaN/Diamond interface parallel to the beam axis were made by focus ion beam machining with Gen 1 material (Fig. 12a). All samples had a pentagonal cross-section to sustain a constant width of the beam near the interface to promote the possibility of interfacial failure over cleavage fracture through the diamond. A notch, of depth $\sim 200 \text{ nm}$, was introduced into the GaN layer close to the fixed end of the cantilever and the actual depth of the notch was measured on fractured cantilever cross-section (Fig. 12b). Two loading cycles were applied: the first cycle was to fracture the notch in the GaN which was marked by a change of the load-displacement curve, and the second loading cycle was to load the cantilever to final failure (Fig. 12b, c). From the first cycle, the fracture toughness of the GaN could be derived and from the second load, by assuming an initial flaw equivalent to the diamond seeds size, the fracture toughness of the polycrystalline diamond substrate can be estimated. Based on these parameters and the final fracture mode (Fig. 10b), the upper bound of the interfacial fracture toughness can be determined from the He and Hutchinson method.⁶⁸

For the measurement of the GaN toughness, the analytical solution proposed by Di Maio and Roberts⁶⁶ on notched pentagonal cantilevers was used:

$$K_{Ic} = \sigma_c \sqrt{\pi a} F\left(\frac{a}{b}\right), \quad (16)$$

where K_{Ic} is the Mode I (stress-intensity based) fracture toughness, and a is the crack length of interest. The fracture stress, σ_c , is calculated from the failure load, P_c , (Fig. 12c) using beam theory. The equations must be adapted for a composite beam of two components (rectangular GaN section, and pentagonal diamond cross-section). An approximate solution was utilized:

$$\sigma_C = \frac{P_C L (\bar{y} - a)}{I_T} , \quad (17)$$

where L is the test length, I_T is the total moment of inertia of the beam, and $(\bar{y} - a)$ gives the distance from the crack tip to the neutral plane. The detailed calculation of these parameters is in Appendix II. $F(a/b)$ in is a geometric factor which can be approximated as the Di Maio and Roberts⁶⁶ factor:

$$F\left(\frac{a}{b}\right) = 1.85 - 3.38\left(\frac{a}{b}\right) + 13.24\left(\frac{a}{b}\right)^2 - 23.26\left(\frac{a}{b}\right)^3 + 16.8\left(\frac{a}{b}\right)^4 . \quad (18)$$

Using above equations and test data (Fig. 12c), the fracture toughness K_{Ic} values for GaN and diamond were calculated to be $1.75 \pm 0.2 \text{ MPa}\cdot\text{m}^{1/2}$ and $4.70 \pm 0.6 \text{ MPa}\cdot\text{m}^{1/2}$, respectively. It worth noting that although no pre-notch was introduced for the diamond, it was assumed to have an initial flaw similar to the seeding particle diameter; indeed, our results are consistent with the literature value of 5-6 $\text{MPa}\cdot\text{m}^{1/2}$.⁶⁷ In addition to the analytical solution based on Di Maio and Roberts,⁶⁶ a finite element (FE) simulation based on continuum model was run on this cantilever experiment (Appendix III) where nonlinear elastic fracture toughness J_{Ic} was derived for GaN and diamond. Equivalent K_{Ic} values were then back-calculated from the J -values assuming the mode-I J - K_I equivalence. The FE analysis gives a K_{Ic} of $3.66 \pm 0.3 \text{ MPa}\cdot\text{m}^{1/2}$ for GaN and $5.40 \pm 0.5 \text{ MPa}\cdot\text{m}^{1/2}$ for the diamond which are nominally consistent with the results derived from the analytical model. Appendix III also includes an example of creating micro-cantilevers based on the blisters; the results are comparable with the notched cantilever geometry.

To derive the toughness of the interface, the He and Hutchinson⁶⁸ analysis based fracture toughness (G_{Ic}) of the diamond can be used (Fig. 13):

$$G_{Ic} = \frac{K_{Ic}^2}{E_1} , \quad (19)$$

where E_1 is the Young's modulus of the diamond. The analysis, shown in Fig. 13a, considers a crack in the top material (GaN) approaching the interface. The crack can arrest at or deflect along the interface, or it can penetrate the material beneath (diamond). For example, in the current experiment a single side deflection occurred at the interface (Fig. 12b) which fits with the solution in Fig. 13b. He and Hutchinson⁶⁸ developed their analytical solution based on the Dundurs' parameter⁶⁹ (details on Dundurs' parameters are included in Appendix I), which describes the elastic mismatch, of the system:

$$\alpha = \frac{E'_1 - E'_2}{E'_1 + E'_2} \quad (20)$$

where E'_i is the plane strain Young's modulus, given by:

$$E'_i = \frac{E_i}{(1 - \nu_i^2)} \quad (21)$$

For the present GaN-on-Diamond material, where the crack direction is from the GaN into the diamond, the first Dundurs' parameter, α , was calculated to be 0.55; if it was *vice versa*, $\alpha = -0.55$. When used with Fig. 13c, interfacial toughness (in energy terms) needs to be more than 0.51 times that of the diamond, *i.e.*, in terms of a stress intensity $\sim 2.5 \text{ MPa}\cdot\text{m}^{1/2}$, for the crack not to deflect at the interface.

4. Discussion

4.1. Experimental parameters for blistering tests

Although FIB sectioning has been often used to measure blister dimensions in literature,^{15,63} it was found in the present work that for GaN-on-Diamond, or presumably for ceramic-ceramic interfaces with small buckle heights, FIB sectioning cannot provide reliable measurements, as shown in Fig. 14. The unreliability of the radius measurements is most likely due to crack closure; removing nearly half the blister allows the crack to relax and close, making it hard to resolve. The buckle height can grow as it becomes less constrained by surrounding material. An extreme example of this is shown in Fig. 14c. AFM and optical measurements, conversely, can provide good agreement for blister radii measurements (Fig. 6b). With optical measurements, interference techniques⁵⁷ and polarised light,⁶³ such as Nomarski contrast, can be used to increase resolution. It is therefore suggested that for GaN-on-Diamond material, AFM, when used with appropriate parameters, can provide the most reliable characterisation of the geometry of buckle/blister.

4.2. Pinned or unpinned

As can be seen from Table 3, the fracture toughness showed a significant difference depending on the choice of the constant, μ , in Eq. (1), *i.e.*, an unpinned condition for a single buckle and a pinned condition assuming a double buckle. However, the data provided by the alternative methods of two-step and micro-cantilever bending suggest that for GaN-on-Diamond, although there is usually a dip at the centre of the indent, it is more reasonable to consider the buckles as ‘unpinned’. This mode must be understood fully to provide the basis for GaN-on-Diamond type of materials. Therefore, a schematic of this phenomenon is shown in Fig. 15 for a film on a substrate structure.

It is emphasised here that the key difference between the two modes is that double buckles occur on loading whereas single buckles occur on unloading.^{15,16} In double buckling (pinned), the crack grows sufficiently far which reduces the buckling stress for the annulus below the indenter tip (σ_i) and edge (σ_p) stresses; *i.e.*, σ_B falls rapidly with increasing crack length (Fig. 7b); the result is that the annulus forms double buckles (Fig. 15c),^{15,16,29} and the cross-section appears as two near-symmetric buckles on either side of the indenter tip.^{15,16,29} Single buckles, conversely, are caused by σ_p on unloading when the indenter tip is being removed, *i.e.*, when the constraint on the film is removed.^{15,16,29} The whole crack acts as one large plate such that σ_B is low and $\sigma_p > \sigma_B$.^{16,29,61} However, double buckles can rebound elastically on unloading and appear unbuckled.^{16,35}

The following are the most agreed criteria for identifying double buckling^{15,16,34,35,63}: double buckles (i) have gradual surface profiles up to the indent, whereas single buckles have sharper profiles, (ii) are symmetric about the centre of the indent, and (iii) have centres that are still in contact with the film. In the present work, the line profiles were all asymmetric and sharp, strongly suggesting unpinned buckling. This argument is additionally supported by the consistency in the results derived using unpinned constant, μ , and that obtained from two-step and micro-cantilever methods. For the FIB slices in Fig. 14, the indent centres appear to have a dip at the centre; however, the buckles are not symmetrical which excludes the possibility for double buckling. It worth noting, though, that when using a Berkovich tip rather than a 90° conical indenter,^{34–36,63} there could be localised compression under the indent which may constrain the centre of the indent from becoming free, but this should not be mistaken as ‘pinned’ double buckling.

4.3. Engineering a stronger interface

From the three types of GaN-on-Diamond materials, a smooth interface appears to lead to an improved TBR_{eff} (see Gen 3 material in Table 1), but reduces the interfacial fracture toughness. On the other hand, introducing zigzag or undulating features to increase fracture surface area is at the cost of the thermal boundary resistance. This is consistent with a decreased phonon scattering at a smoother interface. For an ideal optimised material, a balance between the two aspects needs to be achieved.

Although the current GaN-on-Diamond system has shown improved interfacial stability compared with earlier generations of materials (Table 3 and 4), their toughness is still lower than, for example, GaN grown on Si, where $G_{IC} > 2.96 \pm 0.4 \text{ J}\cdot\text{m}^{-2}$, although it is comparable to the toughness of interfaces where SiN_x is grown on other materials such as GaAs, where $G_I = 0.76 - 2.59 \text{ J}\cdot\text{m}^{-2}$.^{46,48} Diamond, SiN_x and GaN are all covalently bonded; as the diamond particles are sprinkled onto the SiN_x , the SiN_x /diamond seeding particle interface is originally bonded by van der Waals forces, though during the growth process typically carbides and covalent bonds form. In addition, as the interface is incoherent, plastic and elastic discontinuities will almost certainly exist in the interface. Accordingly, we believe that improving the bonding between the SiN_x and the diamond seeds represents a key to enhancing the toughness of the GaN-on-Diamond interface.

One solution to this is to introduce scratches to the SiN_x layer and match the size of the scratches to the seeding-particle size to develop a tougher interface, similar to that in the Gen 2 material. Ohji *et al.*⁷⁰ showed that nano-particles can cause bridging by deflecting the crack around them. Adding larger seeding particles could have a similar effect, as this would induce a tougher interface but without raising the effective thermal boundary resistance. The intent would be to align the larger particles with the scratches to generate crack bridging around linear clusters as seen in the Gen 2 material. To further increase the interfacial toughness, the diamond particles could be embedded into the SiN_x to create intrinsic strong bonds between the two phases together with a mechanical “keying” mechanism at the interface. To achieve this, the seeding layer could be gently ‘compressed’ after ultrasound dispersion. Alternatively, the seeding particles could be introduced during SiN_x growth, although this may not be practical.

However, the prime objective of this study was to assist the development of GaN-on-Diamond materials by assuring the structural integrity of the GaN_x /Diamond interface through an assessment of reliable surface-based approaches to evaluate their interfacial fracture toughness. Suffice to say that, by a comprehensive study combining experimental and analytical methods, the basis for the quantification of interfacial toughness in GaN-on-Diamond materials has been established and can be implemented to new designs in a very straightforward way.

5. Conclusions

A reliable surface-based nano-indentation method for the evaluation of GaN-on-Diamond system has been proposed through systematic experimental measurements and rigorous examination of analytical methods. It is suggested that improving the attachment between the SiN_x and the diamond seeds represents a key to enhancing the toughness of the GaN-on-Diamond interface. There are two primary conclusions:

- Two indentation methods, that involving the development of a blistering from either a single monotonically-loaded indent or a two-step indentation process, are capable of measuring consistent fracture toughness values for interfaces between GaN and Diamond. The Marshall and Evans analysis of indentation-induced buckles was found to be inaccurate for GaN-on-Diamond material, most likely due to the lack of elastic indentation stress considerations.
- For the GaN-on-Diamond interfaces, the mode I fracture toughness (G_{IC}) values were found to be: 0.66 ± 0.2 (monotonic method) and 0.57 ± 0.2 (two-step method) $\text{J}\cdot\text{m}^{-2}$ for Gen 1 material, 0.87 ± 0.1 (monotonic) and 0.91 ± 0.3 (two-step) $\text{J}\cdot\text{m}^{-2}$ for Gen 2 material, and 0.55 ± 0.1 (monotonic) and 0.53 ± 0.2 (two-step) $\text{J}\cdot\text{m}^{-2}$ for Gen 3 material. The Gen 2 material was found to display the toughest interface, which was attributed to the scratched SiN_x matching the seeding particle size.

Supporting Information

Phase angle and interface fracture mechanics; Calculation of the parameters for the centroid and moments of inertia; Linear elastic finite element simulation of micro-cantilever bending.

Acknowledgements

This work was in part supported by the UK Engineering and Physical Science Research Council (EPSRC) under the program grant GaN-DaME (EP/P00945X). DL acknowledges EPSRC for a Research Fellowship (EP/N004493/1) and the Royal Commission for the Exhibition of 1851 for the Brunel Research Fellowship award. Support for ROR was provided by the U.S. Department of Energy, Office of Science, Office of Basic Energy Sciences, Materials Sciences and Engineering Division, under contract no. DE-AC02-05CH11231. The authors acknowledge Prof. James Marrow (Univ. Oxford) for useful discussions and Prof. David Armstrong (Univ. Oxford) for the use of the nanoindenter.

References

1. Sun, H., Simon, R. B., Pomeroy, J. W., Francis, D., Faili, F., Twitchen, D. J. & Kuball, M. Reducing GaN-on-diamond interfacial thermal resistance for high power transistor applications. *Appl. Phys. Lett.* **106**, (2015).
2. Manoi, A., Pomeroy, J. W., Killat, N. & Kuball, M. Benchmarking of thermal boundary resistance in AlGaIn/GaN HEMTs on SiC substrates: Implications of the nucleation layer microstructure. *IEEE Electron Device Lett.* **31**, 1395–1397 (2010).
3. Pomeroy, J. W., Bernardoni, M., Dumka, D. C., Fanning, D. M. & Kuball, M. Low thermal resistance GaN-on-diamond transistors characterized by three-dimensional Raman thermography mapping. *Appl. Phys. Lett.* **104**, (2014).
4. Jessen, G. H., Gillespie, J. K., Via, G. D., Crespo, A., Langley, D., Wasserbauer, J., Faili, F., Francis, D., Babic, D., Ejeckam, F., Guo, S. & Eliashevich, I.. AlGaIn/GaN HEMT on diamond technology demonstration. *Tech. Dig. - IEEE Compd. Semicond. Integr. Circuit Symp. CSIC 271–274* (2006).
5. Dumka, D. C. & Saunier, P. AlGaIn/GaN HEMTs on diamond substrate. *65th DRC Device Res. Conf.* **25**, 31–32 (2007).
6. Tyhach, M., Altman, D., Bernstein, S., Korenstein, R., Cho, J., Goodson, K. E., Francis, D., Faili, F., Ejeckam, F., Kim, S. & Graham, S. S2-T3: Next generation gallium nitride HEMTs enabled by diamond substrates. *Lester Eastman Conf. 2014 - High Perform. Devices, LEC 2014* (2014).
7. Ejeckam, F., Francis, F., Firooz, F., Twitchen, D., Bolliger, B., Babic, D. & Felbinger, J. GaN-on-diamond: A brief history. *2014 Lester Eastman Conf. High Perform. Devices 1–5* (2014).
8. Chao, P.-C., Chu, K., Creamer, C., Diaz, J., Yurovchak, T., Shur, M., Kallaher, R., McGray, C., Via, G. D. & Blevins, J. D. Low-Temperature Bonded GaN-on-Diamond HEMTs With 11 W/mm Output Power at 10 GHz. *IEEE Trans. Electron Devices* **62**, 3658–3664 (2015).
9. Van Dreumel, G. W. G., Tinnemans, P. T., Van Den Heuvel, A. A. J., Bohnen, T., Buijnsters, J. G., Ter Meulen, J. J., Van Enckevort, W. J. P., Hageman, P. R. & Vlieg, E. Realising epitaxial growth of GaN on (001) diamond. *J. Appl. Phys.* **110**, (2011).
10. Hirama, K., Kasu, M. & Taniyasu, Y. RF high-power operation of AlGaIn/GaN HEMTs epitaxially grown on diamond. *IEEE Electron Device Lett.* **33**, 513–515 (2012).
11. Alomari, M., Martin, D., Grandjean, N., Gaquiere, C. & Kohn, E. AlGaIn/GaN HEMT on (111) single crystalline diamond. *Electron. Lett.* **46**, 299 (2010).
12. Cho, J., Francis, D., Altman, D. H., Asheghi, M. & Goodson, K. E. Phonon conduction in GaN-diamond composite substrates. *J. Appl. Phys.* **121**, (2017).

13. Francis, D., Faili, F., Babi, D., Ejeckam, F., Nurmikko, A. & Maris, H. Formation and characterization of 4-inch GaN-on-diamond substrates. **19**, 229–233 (2010).
14. Dumka, D. C., Francis, D., Chou, T. M., Ejeckam, F. & Faili, F. AlGaIn/GaN HEMTs on diamond substrate with over 7 W/mm output power density at 10 GHz. *Electron. Lett.* **49**, 1298–1299 (2013).
15. Gerberich, W. W. & Cordill, M. J. Physics of adhesion. *Reports Prog. Phys.* **69**, 2157–2203 (2006).
16. Volinsky, A. ., Moody, N. . & Gerberich, W. . Interfacial toughness measurements for thin films on substrates. *Acta Mater.* **50**, 441–466 (2002).
17. Wang, X., Wang, C. & Atkinson, A. Interface fracture toughness in thermal barrier coatings by cross-sectional indentation. *Acta Mater.* **60**, 6152–6163 (2012).
18. Zhao, P. F., Sun, C. A., Zhu, X. Y., Shang, F. L. & Li, C. J. Fracture toughness measurements of plasma-sprayed thermal barrier coatings using a modified four-point bending method. *Surf. Coatings Technol.* **204**, 4066–4074 (2010).
19. Hofinger, I., Oechsner, M., Bahr, H. & Swain, M. V. Modified four-point bending specimen for determining the interface fracture energy for thin , brittle layers. *Int. J. Fract.* **92**, 213–220 (1998).
20. Eberl, C., Wang, X., Gianola, D. S., Nguyen, T. D., He, M. Y., Evans, A. G. & Hemker, K. J. In situ measurement of the toughness of the interface between a thermal barrier coating and a Ni alloy. *J. Am. Ceram. Soc.* **94**, 120–127 (2011).
21. Dauskardt, R. H., Lane, M., Ma, Q. & Krishna, N. Adhesion and debonding of multi-layer thin film structures. *Eng. Fract. Mech.* **61**, 141–162 (1998).
22. Volinsky, A. A., Vella, J. B. & Gerberich, W. W. Fracture toughness, adhesion and mechanical properties of low-K dielectric thin films measured by nanoindentation. *Thin Solid Films* **429**, 201–210 (2003).
23. Charalambides, P. G., Lund, J., Evans, A. G. & McMeeking, R. M. A test specimen for determining the fracture resistance of bimaterial interfaces. *J. Appl. Mech.* **56**, 77 (1989).
24. Charalambides, P. G., Cao, H. C., Lund, J. & Evans, a G. Developement of a test method for measuring the mixed mode fracture resistance of bimaterial interfaces. **8**, 269–283 (1990).
25. Atkinson, C., Smelser, R. E. & Sanchez, J. Combined mode fracture via the cracked Brazilian disk test. **18**, 279–291 (1980).
26. Wang, J. S. & Suo, Z. Experimental determination of interfacial toughness curves using Brazil-nut-sandwiches. *Acta Metall. Mater.* **38**, 1279–1290 (1990).
27. Ma, Q. A four-point bending technique for studying subcritical crack growth in thin films and at interfaces. *J. Mater. Res.* **12**, 840–845 (1997).
28. Dannenberg, H. Measurement of adhesion by a blister method. **V**, 125–134 (1961).
29. Chen, J. & Bull, S. J. Approaches to investigate delamination and interfacial toughness in coated systems: an overview. *J. Phys. D: Appl. Phys.* **44**, 034001 (2011).
30. Bagchi, A., Lucas, G. E., Suo, Z. & Evans, A. G. A new procedure for measuring the decohesion energy for thin ductile films on substrates. (2017).
31. Marshall, D. B. & Evans, A. G. Measurement of adherence of residually stressed thin films by indentation. I. Mechanics of interface delamination. *J. Appl. Phys.* **56**, 2632–2638 (1984).
32. Kriese, M. D., Gerberich, W. W. & Moody, N. R. Quantitative adhesion measures of multilayer

- films: Part I. Indentation Mechanics. *J. Mater. Res.* (1999).
33. Cordill, M. J., Bahr, D. F., Moody, N. R. & Gerberich, W. W. Adhesion measurements using telephone cord buckles. *Mater. Sci. Eng. A* **443**, 150–155 (2007).
 34. Kleinbichler, A., Pfeifenberger, M. J., Zechner, J., Moody, N.R., New insights into nanoindentation-based adhesion testing. *JOM* **69** (11), 2237–2245 (2017).
 35. Kleinbichler, A., Zechner, J. & Cordill, M. J. Buckle induced delamination techniques to measure the adhesion of metal dielectric interfaces. *Microelectron. Eng.* **167**, 63–68 (2017).
 36. Waters, P. & Volinsky, A. A. Stress and moisture effects on thin film buckling delamination. *Exp. Mech.* **47**, 163–170 (2007).
 37. Volinsky, A., Moody, N. R. & Gerberich, W. W. Superlayer residual stress effect on the indentation adhesion measurements. *Mater. Res. Soc. Symp. - Proc.* (2000).
 38. Kuzel, R., Valvoda, V., Chladek, M., Musil, J. & Matous, J. XRD microstructural study of Zn films deposited by unbalanced magnetron sputtering. *Thin Solid Films* **263**, 150–158 (1995).
 39. Sciences, A. Magnetron Sputtering Deposition – magnetron sputtered thin films. 15110 (2017).
 40. Chang, J. ., Shen, C. . & Hon, M. . Growth characteristics and residual stress of RF magnetron sputtered ZnO:Al films. *Ceram. Int.* **29**, 245–250 (2003).
 41. Kelly, P. J. & Arnell, R. D. Magnetron sputtering: a review of recent developments and applications. *Vacuum* **56**, 159–172 (2000).
 42. Sanchez, J., El-Mansy, S., Sun, B., Scherban, T., Fang, N., Pantuso, D., Ford, W., Elizalde, M., Martinez-Esnaola, J., Martin-Meizoso, A., Gil-Sevillano, J., Fuentes, M. & Maiz, J. Cross-sectional nanoindentation: a new technique to measure thin film interfacial adhesion. *Acta Metall.* **47**, 3–8 (1999).
 43. Boer, M. P. D. E. & Gerberich, W. W. Microwedge indentation of the thin film line-i. mechanics. **44**, (1996).
 44. Boer, M. P. D. E. & Gerberich, W. W. Microwedge indentation of the thin film fine line - II. Experiment. *Acta Metall.* **44**, 3177–3187 (1996).
 45. Hainsworth, S. ., McGurk, M. . & Page, T. The effect of coating cracking on the indentation response of thin hard-coated systems. *Surf. Coatings Technol.* **102**, 97–107 (1998).
 46. Xie, H. & Huang, H. Characterization of the interfacial strength of SiNx/GaAs film/substrate systems using energy balance in nanoindentation. *J. Mater. Res.* **28**, 3137–3145 (2013).
 47. Lu, M. & Huang, H. Interfacial energy release rates of SiN/GaAs film/substrate systems determined using a cyclic loading dual-indentation method. *Thin Solid Films* **589**, 822–830 (2015).
 48. Lu, M. & Huang, H. Determination of the energy release rate in the interfacial delamination of silicon nitride film on gallium arsenide substrate via nanoindentation. *J. Mater. Res.* **29**, 801–810 (2014).
 49. Wei, P. J., Liang, W. L., Ai, C. F. & Lin, J. F. A new method for determining the strain energy release rate of an interface via force-depth data of nanoindentation tests. *Nanotechnology* **20**, (2009).
 50. Zhou, Y., Ramaneti, R., Anaya, J., Korneychuk, S., Derluyn, J., Sun, H., Pomeroy, J., Verbeeck, J., Haenen, K. & Kuball, M. Thermal characterization of polycrystalline diamond thin film heat spreaders grown on GaN HEMTs. *Appl. Phys. Lett.* **111**, (2017).

51. Williams, O. A., Nesladek, M., Daenen, M., Michaelson, S., Hoffman, A., Osawa, E., Haenen, K. & Jackman, R. B. Growth, electronic properties and applications of nanodiamond. *Diam. Relat. Mater.* **17**, 1080–1088 (2008).
52. Twitchen, D. J., Sun, H., Liu, D., Pomeroy, J. W., Francis, D., Faili, F., Twitchen, D. J. & Kuball, M. GaN-on-diamond : Robust mechanical and thermal properties GaN-on-diamond : Robust mechanical and thermal properties. in 201–204 (2016).
53. Oliver, W. C. & Pharr, G. M. An improved technique for determining hardness and elastic modulus using load and displacement sensing indentation experiments. *J. Mater. Res.* **7**, 1564–1583 (1992).
54. Tsai, C. H., Jian, S. R. & Juang, J. Y. Berkovich nanoindentation and deformation mechanisms in GaN thin films. *Appl. Surf. Sci.* **254**, 1997–2002 (2008).
55. Nowak, R., Pessa, M., Suganuma, M., Leszczynski, M., Grzegory, I., Porowski, S., & Yoshida, F. Elastic and plastic properties of GaN determined by nano-indentation of bulk crystal Elastic and plastic properties of GaN determined by nano-indentation of bulk crystal. *Appl. Phys. Lett.* **75**, 18–21 (1999).
56. Nečas, D. & Klapetek, P. Gwyddion: An open-source software for SPM data analysis. *Cent. Eur. J. Phys.* **10**, 181–188 (2012).
57. Rossington, C., Evans, A. G., Marshall, D. B. & Khuri-Yakub, B. T. Measurements of adherence of residually stressed thin films by indentation. II. Experiments with ZnO/Si. *J. Appl. Phys.* **56**, 2639–2644 (1984).
58. Lawn, B. R., Evans, A. & Marshall, D. B. Elastic / Plastic indentation damage in ceramics : The lateral crack system. *J. Am. Ceram. Soc.* **63**, 574–581 (1980).
59. Chen, X., Hutchinson, J. W. & Evans, A. G. The mechanics of indentation induced lateral cracking. *J. Am. Ceram. Soc.* **88**, 1233–1238 (2005).
60. Evans, A. G. & Hutchinson, J. W. On the mechanics of delamination and spalling in compressed films. *Int. J. Solids Struct.* **20**, 455–466 (1984).
61. Hutchinson, J. W. & Suo, Z. Mixed mode cracking in layered materials. *Adv. Appl. Mech.* **29**, 63–191 (1992).
62. Caldas, P. G., Silva, E. M., Prioli, R., Huang, J. Y., Juday, R., Fischer, A. M. & Ponce, F. A. Plasticity and optical properties of GaN under highly localized nanoindentation stress fields. *J. Appl. Phys.* **121**, (2017).
63. Cordill, M. J., Bahr, D. F., Moody, N. R. & Gerberich, W. W. Recent developments in thin film adhesion measurement. *IEEE Trans. Device Mater. Reliab.* **4**, 163–168 (2004).
64. Swanson, P. L., Fairbanks, C. J., Lawn, B. R., Mai, Y.-W & Hockey, B. J. Crack-interface grain bridging as a fracture resistance I, Mechanism in ceramics: I, Experimental study on alumina. *J. Am. Ceram. Soc.* **70**, 279–289 (1987).
65. Miyazato, T., Hojo, M., Sugano, M., Adachi, T., Inoue, Y., Shikimachi, K., Hirano, N. & Nagaya, S. Mode I type delamination fracture toughness of YBCO coated conductor with additional Cu layer. *Phys. C Supercond. its Appl.* **471**, 1071–1074 (2011).
66. Di Maio, D. & Roberts, S. G. Measuring fracture toughness of coatings using focused-ion-beam-machined microbeams. *J. Mater. Res.* **20**, 299–302 (2005).
67. Drory, M. D., Dauskardt, R. H., Kant, A. & Ritchie, R. O. Fracture of synthetic diamond. *J. Appl. Phys.* **78**, 3083–3088 (1995).
68. He, M. & Hutchinson, J. W. Crack Deflection at an interface between dissimilar elastic

- 1
2
3 materials. *Int. J. Solids Struct.* **25**, 1053–1067 (1989).
4
5 69. Dundurs, J. Discussion: Edge-bonded dissimilar orthogonal elastic wedges under normal and
6 shear loading. *J. Appl. Mech.* **36**, 650–652 (1969).
7
8 70. Ohji, T., Jeong, Y.-K., Choa, Y.-H. & Niihara, K. Strengthening and Toughening Mechanisms of
9 Ceramic Nanocomposites. *J. Am. Ceram. Soc.* **60**, 1453–1460 (1998).
10
11
12
13
14
15
16
17
18
19
20
21
22
23
24
25
26
27
28
29
30
31
32
33
34
35
36
37
38
39
40
41
42
43
44
45
46
47
48
49
50
51
52
53
54
55
56
57
58
59
60

List of Figure Captions

Fig. 1: Schematic of the main steps for processing a GaN-on-Diamond wafer.

Fig. 2: (a) A typical indentation load-displacement curve, showing the two hold periods; (b) arrays of indentation-induced blisters on a Gen 1 wafer; (c) a typical load-time curve, and (d) the segmentation of the work of delamination for the two-step method.

Fig. 3: (a) FIB methods used to make pentagonal cantilever cross-sections. Further polishing steps and notching were carried out after stages shown in (a). (b) The scanned cantilever, loading position (marked by the blue cross), and testing parameters. Triangle shows tip orientation in testing.

Fig. 4: The process for segmenting the buckle width and height in AFM. (a) an AFM image and the height profile as a function of distance across the blister; (b) a 'qualified' blister/buckle with the protective layer chipping, and (c) an "invalid" blister with large scale cracking.

Fig. 5: Comparison of the blister radius measured by (a) AFM and optical and by (b) AFM, optical with FIB sectioning; (c) the blister radius, and (d) blister height are plotted as a function of maximum load (mN).

Fig. 6: (a) ME analysis steps (Reproduced with permission from reference 31. Copyright 2019 AIP Publishing). (1) to (3) show dilatations from residual and indentation stress, (4) shows the resulting edge compression; (b) the calculated indentation edge stresses and the critical buckling stress.

Fig. 7: (a) G_{Ic} values derived from the Hutchinson and Suo (HS) method: the circled region is the valid toughness values used for the plot in (b); (b) population histograms of the values used for calculating the average fracture toughness.

Fig. 8: Typical load-unload displacement curves for (a) Gen 2 GaN-on-Diamond samples and (b) corresponding Gen 1 and Gen 3 materials; (c) the delamination radii and (d) the work of delamination as a function of maximum load for the two-step method.

Fig. 9: (a) Mode I toughness G_{Ic} at the interface estimated using the two-step indentation method; comparison of the crack radius as a function of the maximum indenter load based on the two-step and monotonic crack length methods for the (b) Gen 1, (c) Gen 2 and (d) Gen 3 GaN-on-Diamond materials.

Fig. 10: The cross-sectional images showing the typical fracture pattern in (a) Gen 1, (b) Gen 2 and (c) Gen 3 materials. Note the fracture patterns in (a) and (c) are both present in Gen 3 material.

Fig. 11: Spalled surface for (a) Gen 1, (b) Gen 2, and (c) Gen3 materials. (a.1) showing pin holes and (a.2) shows the TEM cross-sectional image of Gen 1 material; (b.1) is a higher magnification image of (b) showing a mixture of diamond substrate (Dia.), SiN_x and diamond particles (DP) and (b.2) shows the TEM cross-sectional image of Gen 2 material; (c.1) is a blown-up of (c) and (c.2) shows the TEM cross-sectional image of Gen 3 material.

Fig. 12: (a) Notched cantilever; (b) fractured cantilever after loading cycles shown in (c).

Fig. 13: (a) A crack running from material 1 (GaN) and impinging on the interface with material 2 (diamond) can either (a) penetrate or (b) arrest or deflect. (c) Diagram illustrates He and Hutchinson's linear-elastic analytical solution where whether a crack impinging on a dissimilar material interface penetrates or arrests is a function of the modulus mismatch across the interface, defined by the first Dundurs' parameter α , the interfacial (energetic) toughness G_{Ic} and the (energetic) toughness of material 2 (diamond) G_{Ic} .

Fig. 14: (a) A typical example demonstrating the difference in the crack length measured using SEM/FIB, as compared to measurements using AFM and optical microscopy; (c) shows the rebounded crack in (b) after further sectioning.

Fig. 15: The different processes between (a) double pinned buckling and (b) single unpinned buckling.

1
2
3
4
5
6
7
8
9
10
11
12
13
14
15
16
17
18
19
20
21
22
23
24
25
26
27
28
29
30
31
32
33
34
35
36
37
38
39
40
41
42
43
44
45
46
47
48
49
50
51
52
53
54
55
56
57
58
59
60

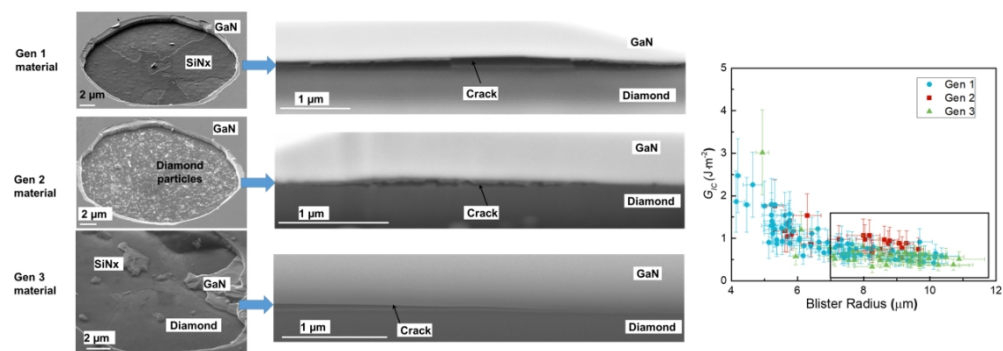


Table of Contents Graphic

338x190mm (96 x 96 DPI)

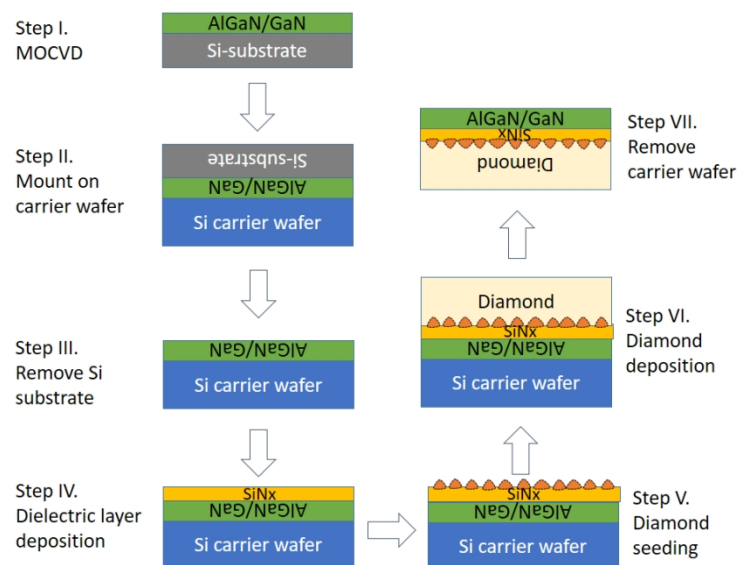


Fig. 1: Schematic of the main steps for processing a GaN-on-Diamond wafer.

338x190mm (96 x 96 DPI)

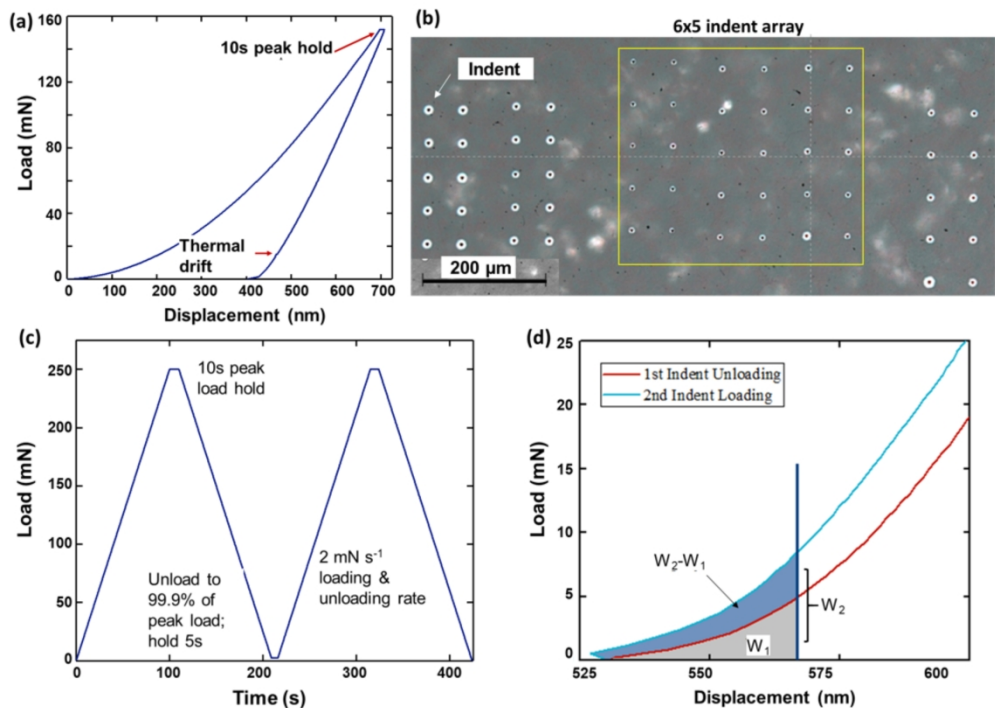


Fig. 2: (a) A typical indentation load-displacement curve, showing the two hold periods; (b) arrays of indentation-induced blisters on a Gen 1 wafer; (c) a typical load-time curve, and (d) the segmentation of the work of delamination for the two-step method.

263x187mm (289 x 289 DPI)

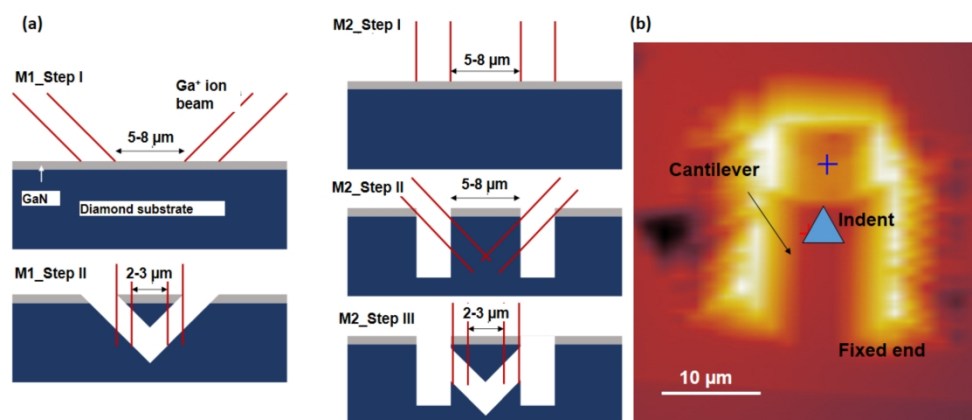


Fig. 3: (a) FIB methods used to make pentagonal cantilever cross-sections. Further polishing steps and notching were carried out after stages shown in (a). (b) The scanned cantilever, loading position (marked by the blue cross), and testing parameters. Triangle shows tip orientation in testing.

338x151mm (293 x 293 DPI)

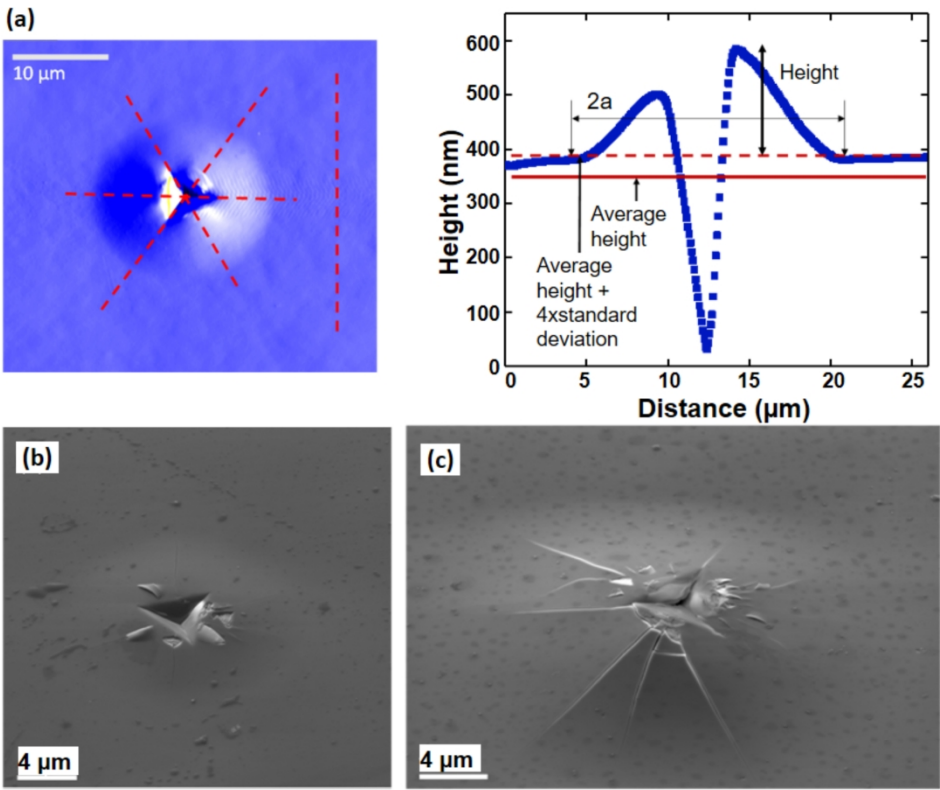


Fig. 4: The process for segmenting the buckle width and height in AFM. (a) an AFM image and the height profile as a function of distance across the blister; (b) a 'qualified' blister/buckle with the protective layer chipping, and (c) an "invalid" blister with large scale cracking.

241x190mm (300 x 300 DPI)

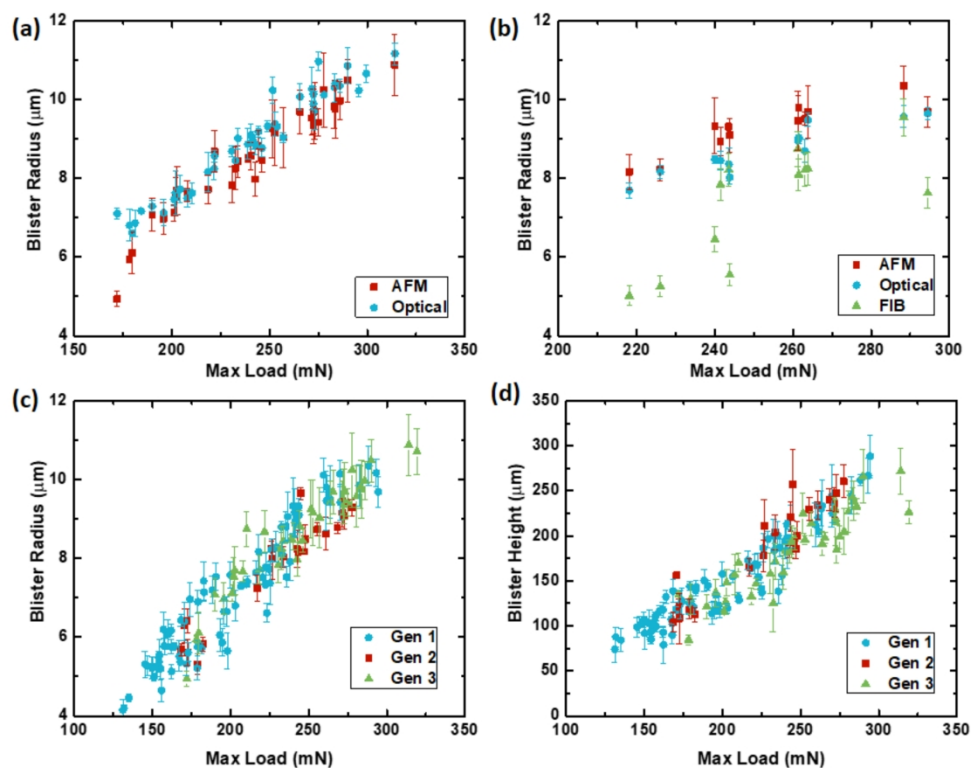


Fig. 5: Comparison of the blister radius measured by (a) AFM and optical and by (b) AFM, optical with FIB sectioning; (c) the blister radius, and (d) blister height are plotted as a function of maximum load (mN).

242x189mm (300 x 300 DPI)

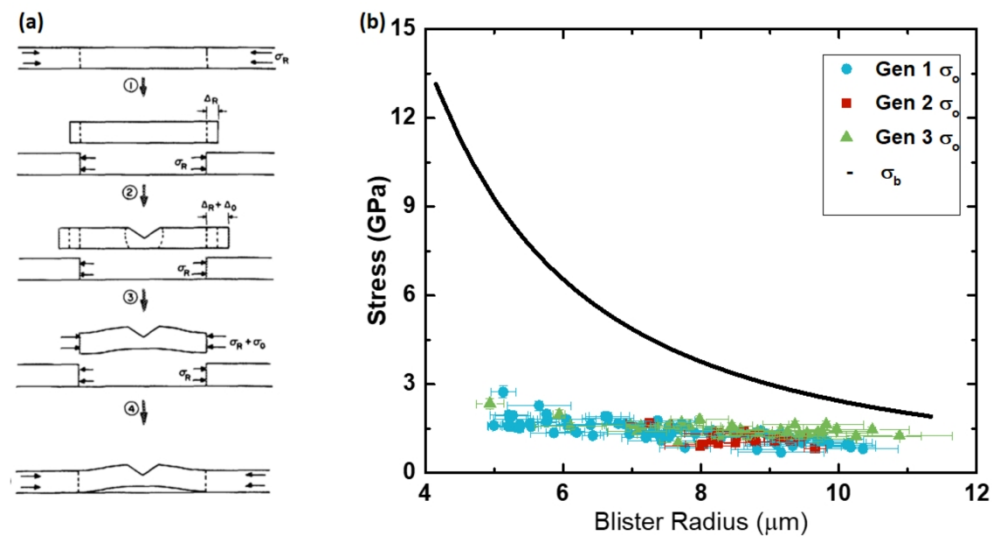


Fig. 6: (a) ME analysis steps (Reproduced with permission from reference 31. Copyright 2019 AIP Publishing). (1) to (3) show dilatations from residual and indentation stress, (4) shows the resulting edge compression; (b) the calculated indentation edge stresses and the critical buckling stress.

307x166mm (297 x 297 DPI)

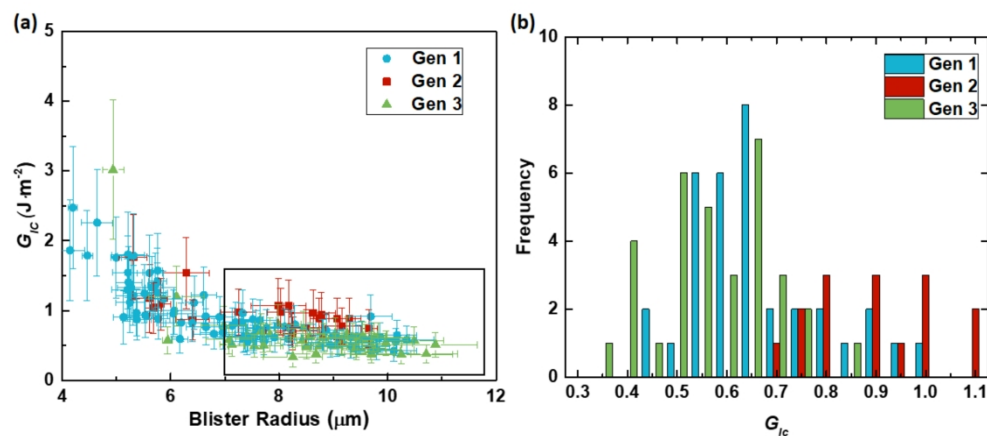


Fig. 7: (a) G_{IC} values derived from the Hutchinson and Suo (HS) method: the circled region is the valid toughness values used for the plot in (b); (b) population histograms of the values used for calculating the average fracture toughness.

323x143mm (283 x 283 DPI)

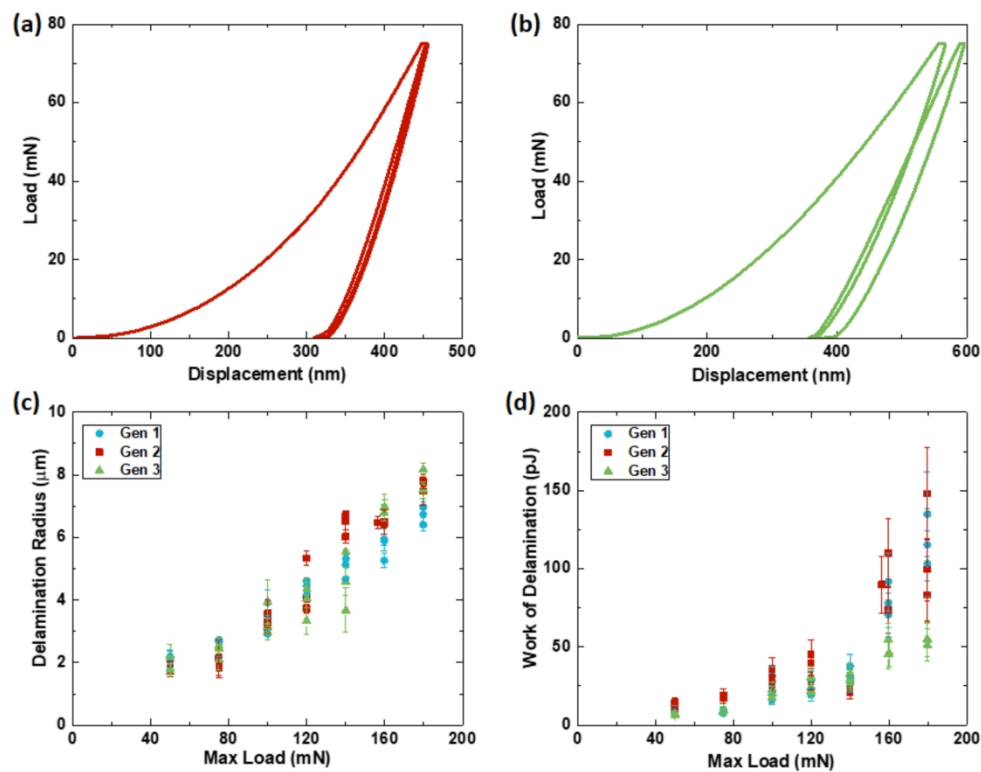


Fig. 8: Typical load-unload displacement curves for (a) Gen 2 GaN-on-Diamond samples and (b) corresponding Gen 1 and Gen 3 materials; (c) the delamination radii and (d) the work of delamination as a function of maximum load for the two-step method.

237x185mm (299 x 299 DPI)

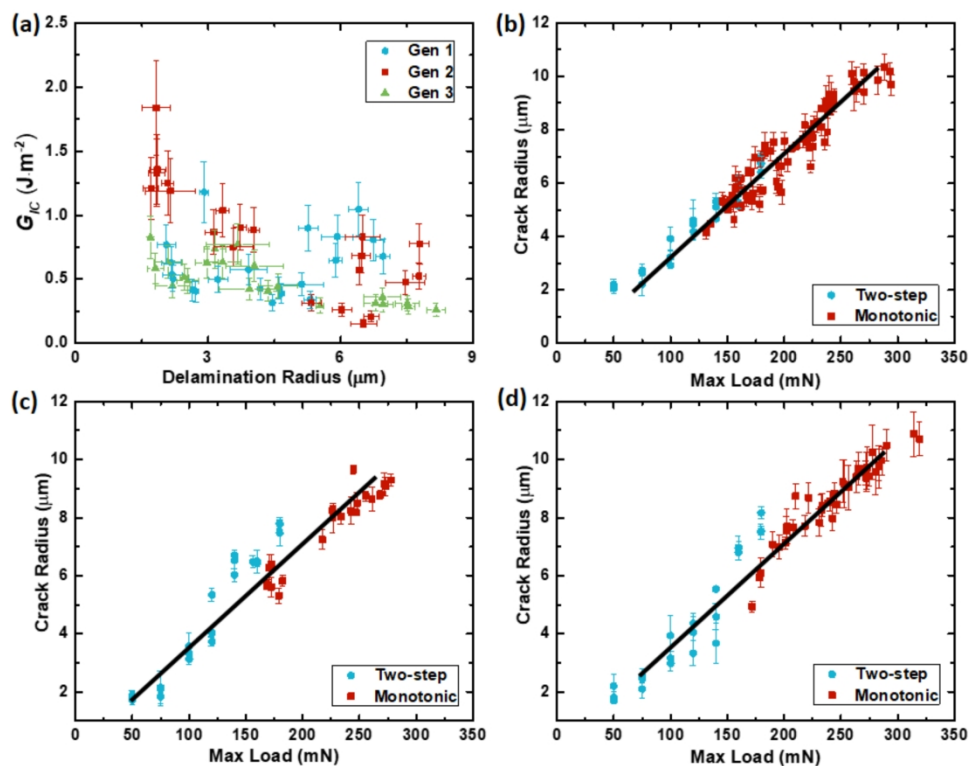


Fig. 9: (a) Mode I toughness G_{IC} at the interface estimated using the two-step indentation method; comparison of the crack radius as a function of the maximum indenter load based on the two-step and monotonic crack length methods for the (b) Gen 1, (c) Gen 2 and (d) Gen 3 GaN-on-Diamond materials.

243x189mm (292 x 292 DPI)

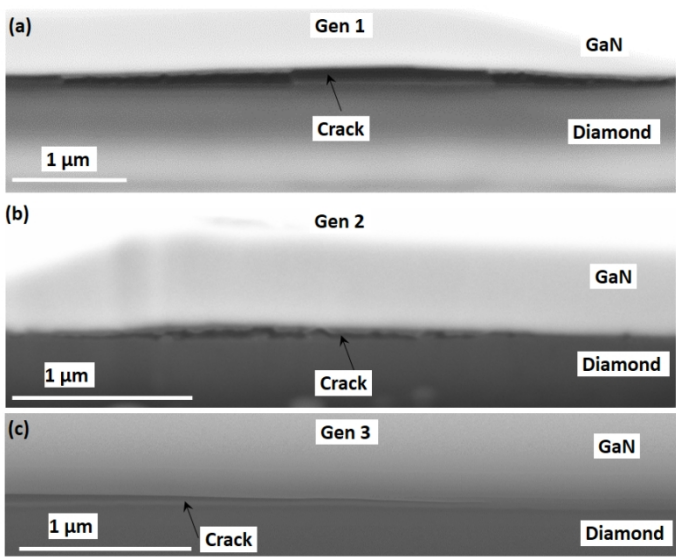


Fig. 10: The cross-sectional images showing the typical fracture pattern in (a) Gen 1, (b) Gen 2 and (c) Gen 3 materials. Note the fracture patterns in (a) and (c) are both present in Gen 3 material.

338x190mm (96 x 96 DPI)

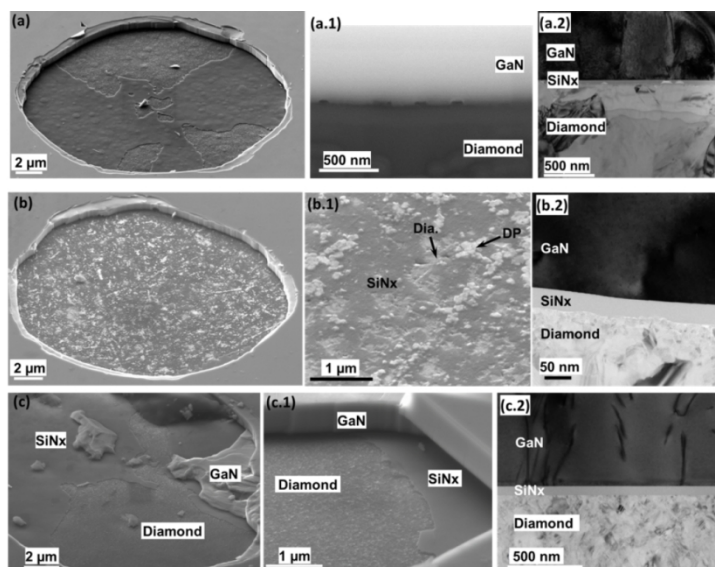


Fig. 11: Spalled surface for (a) Gen 1, (b) Gen 2, and (c) Gen3 materials. (a.1) showing pin holes and (a.2) shows the TEM cross-sectional image of Gen 1 material; (b.1) is a higher magnification image of (b) showing a mixture of diamond substrate (Dia.), SiNx and diamond particles (DP) and (b.2) shows the TEM cross-sectional image of Gen 2 material; (c.1) is a blown-up of (c) and (c.2) shows the TEM cross-sectional image of Gen 3 material.

337x189mm (113 x 113 DPI)

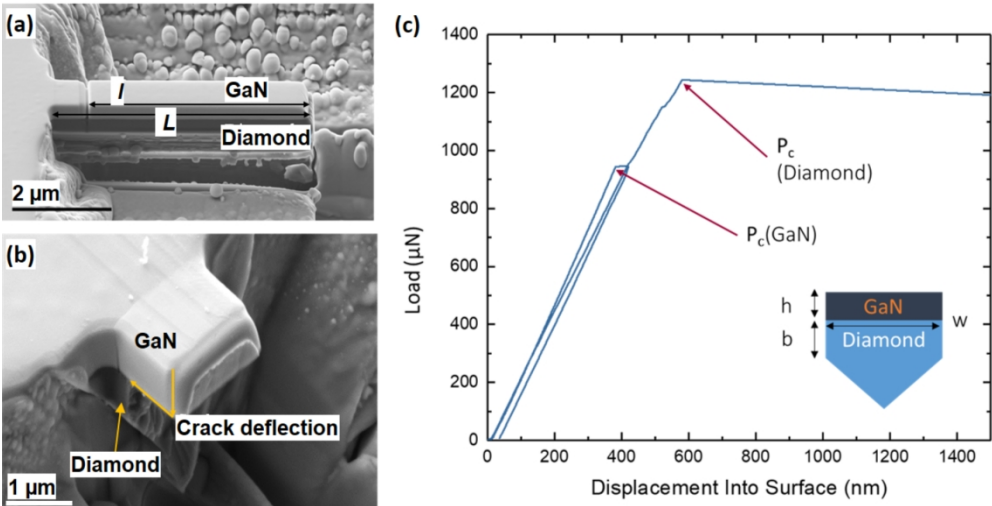


Fig. 12: (a) Notched cantilever; (b) fractured cantilever after loading cycles shown in (c).

338x190mm (150 x 150 DPI)

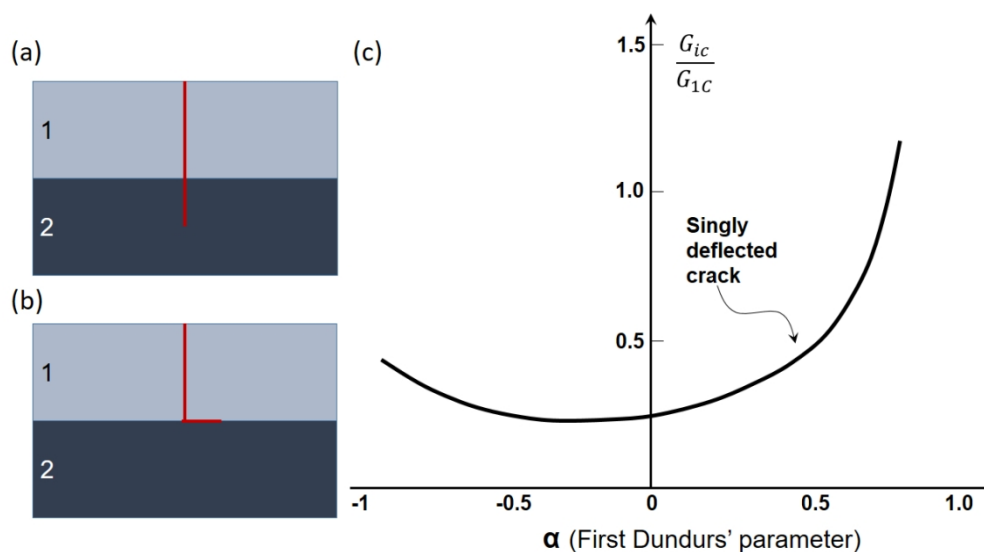


Fig. 13: (a) A crack running from material 1 (GaN) and impinging on the interface with material 2 (diamond) can either (a) penetrate or (b) arrest or deflect. (c) Diagram illustrates He and Hutchinson's linear-elastic analytical solution where whether a crack impinging on a dissimilar material interface penetrates or arrests is a function of the modulus mismatch across the interface, defined by the first Dundurs' parameter α , the interfacial (energetic) toughness G_{ic} and the (energetic) toughness of material 2 (diamond) G_{1c} .

338x190mm (96 x 96 DPI)

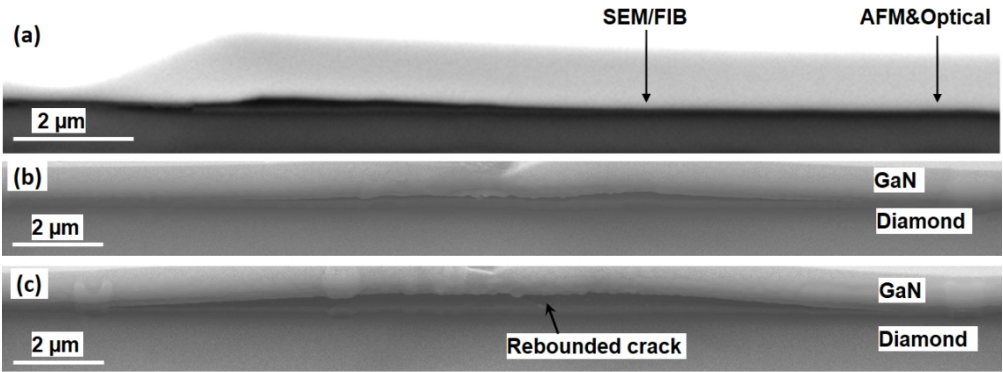


Fig. 14: (a) A typical example demonstrating the difference in the crack length measured using SEM/FIB, as compared to measurements using AFM and optical microscopy; (c) shows the rebounded crack in (b) after further sectioning.

338x190mm (96 x 96 DPI)

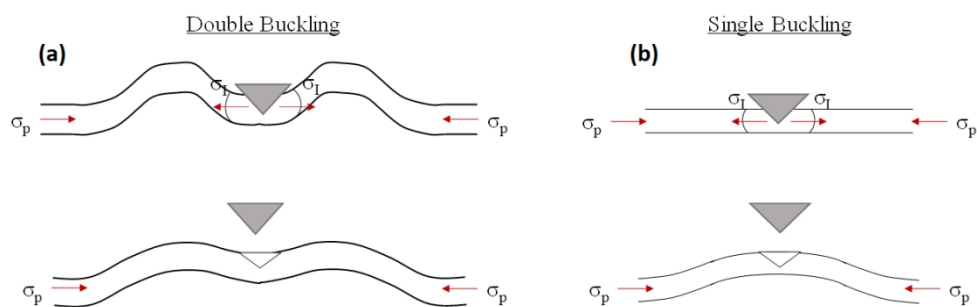


Fig. 15: The different processes between (a) double pinned buckling and (b) single unpinned buckling.

338x190mm (96 x 96 DPI)

Tables

Table 1: Interface properties of the three generations of GaN-on-Diamond tested (refs. 1 and 53)

Materials (Gen no.)	SiN thickness (nm)	Diamond Seeding Particle Size (nm)	Residual Stress in GaN (MPa)	TBR _{eff} / m ² K GW ⁻¹
1	50	~100	400	33
2	36	~50	100	22
3	41	~30	100	15

Table 2: ANOVA analysis of the three populations (DF is the degrees of freedom, SS is the variance, MS = SS/DF).

Source of Variation	SS	DF	MS	F	P-value	F _{crit}
Between Groups	1.08	2	0.54	27.96	6.19x10 ⁻¹⁰	3.11
Within Groups	1.54	80	0.02			
Total	2.62	82				

Table 3: Average G_{Ic} fracture toughness (in kJ·m⁻²) of the interface and associated errors.

Generation of GaN-on-Diamond	1	2	3
No. of indents	35	15	33
Un-pinned	0.66 ± 0.2	0.87 ± 0.1	0.55 ± 0.1
Pinned	5.57 ± 1.5	7.36 ± 1.1	4.63 ± 1

Table 4: Summary of the two-step fracture toughness calculations.

Materials (Gen no.)	$G_{Ic}(\psi)$ (J·m ⁻²)	$G_{Id}(\psi)$ error (J·m ⁻²)	c/R_p Average	d/R_p Average	Phase Angle (degrees)	G_{Ic} (J·m ⁻²)	G_{Ic} error (J·m ⁻²)
1	0.61	0.1	1.87	0.45	20	0.57	0.2
2	0.96	0.2	1.82	0.44	18	0.91	0.3
3	0.56	0.1	1.30	0.34	20	0.53	0.2

Table 5: ANOVA analysis of two-step analysis results.

Source of Variation	SS	DF	MS	F	P-value	F _{crit}
Between Groups	1.385	2	0.693	7.681	0.0013	3.195
Within Groups	4.238	47	0.090			
Total	5.623	49				